RSC Advances

PAPER

View Article Online
View Journal | View Issue

Check for updates

Cite this: *RSC Adv.*, 2024, **14**, 18367

3D flower-like bimetallic Ni–Co metal–organic framework as an electrocatalyst for the oxygen evolution reaction†

Chao Shuai, *[ab] Chao Kong, [ab] Yingying Li,[ab] Liang Zhang, [ab] Caiju Qi[a] and Zunli Mo *[c]

Received 25th March 2024
Accepted 25th May 2024

DOI: 10.1039/d4ra02280g

rsc.li/rsc-advances

The rational design and facile preparation of a catalyst with high activity, strong durability and low consumption for the oxygen evolution reaction (OER) is an ongoing challenge in water splitting to generate clean and renewable H_2 fuel. Herein, bimetallic metal–organic frameworks (MOFs) with a uniform morphology, controlled metal ratio and low crystallinity were constructed using a simple and reliable one-step solvothermal method. The three-dimensional (3D) flower-like MOF (F-Ni1Co4-BTC) with a Ni to Co molar ratio of 1 : 4 coordinated with 1,3,5-benzenetricarboxylic acid exhibited excellent OER catalytic activity compared with its corresponding counterparts, which can be attributed to the establishment of the exquisite morphology, the proportion of the dual-metal center, and the formation of active intermediates. Furthermore, when F-Ni1Co4-BTC was directly grown on carbon cloth (F-Ni1Co4-BTC/CC), it achieved an obvious improvement in electrochemical performance, affording a low overpotential of 292 mV at a current density of 10 mA cm^{-2}, a small Tafel slope (48 mV dec^{-1}), and excellent mechanical durability in an alkaline electrolyte, which is due to the integrated electrode attained richer active sites and faster electron transfer rate with the introduction of highly conductive carbon cloth. Our work offers a promising strategy to tailor the properties of bimetallic MOFs and the possibility of highly efficient earth-abundant catalysts for practical applications.

Introduction

The oxygen evolution reaction (OER), an important half reaction, determines the efficiency of renewable energy technologies, such as water electrolysers and metal–air batteries.[1–3] The inherent sluggishness of the multi-step proton-coupled electron transfer process and rigid O–O double bond formation lead to the sluggish kinetics and high potential of the OER.[4–6] Therefore, an advanced OER electrocatalyst is exploited to solve these issues.[7,8] Up to now, the benchmark electrocatalyst of the OER is noble-metal-based materials (such as Pt-, Ir- and Ru-based compounds). However, their poor stability and high cost seriously impede their commercial application.[9–11] Therefore, developing OER catalysts with low cost, high activity, and strong durability based on earth-abundant metals is imperative for improving the conversion efficiency of renewable energy technologies.[12,13] In particular, the intrinsic activities of first-row transition metal-based OER catalysts have a close connection with the number of 3d electrons from the metal. The e_g orbitals coming from the surface transition-metal ions can bond with surface-anion adsorbates and then determine the binding of oxygenic intermediates.[14,15]

Metal–organic frameworks (MOFs), a new class of crystalline materials, are constructed *via* the formation of coordination bonds between metal clusters or ions and organic ligands.[16,17] In the past decade, most MOF-derived materials have been intensively studied in many areas, such as catalysis, energy storage and conversion, and wastewater treatment, owing to their highly ordered porous structures, large surface areas, and controllable pore sizes.[18–21] However, metal active sites are closely confined in crystalline frameworks, which cannot directly act as efficient catalysts.[22,23] Recently, to solve the above-mentioned issues, the design of an efficient nanostructure and morphology was applied to construct efficient MOF catalysts. For instance, Mai and co-workers efficiently controlled the nanosize and morphology of Fe-BDC MOFs by introducing Ni ions into their structure, resulting in lower crystallinity and smaller crystal sizes compared with monometallic Fe-BDC, which was beneficial in exposing rich active sites, which was attributed to the fact that the incorporation of other metals into the framework can adjust host–guest geometries.[21,24] Zhao and

---

[a] *College of Petroleum and Chemical Engineering, Longdong University, Qingyang 745000, China. E-mail: shuai_xc@163.com*

[b] *Gansu Key Laboratory of Efficient Utilization of Oil and Gas Resources in Longdong, Qingyang, 745000, China*

[c] *Key Laboratory of Polymer Materials of Gansu Province, College of Chemistry and Chemical Engineering, Northwest Normal University, Lanzhou 730070, People's Republic of China. E-mail: mozlnwnu@126.com*

† Electronic supplementary information (ESI) available. See DOI: https://doi.org/10.1039/d4ra02280g

co-workers developed a facile ultrasonic stripping strategy to convert traditional bulk MOFs into an ultrathin two-dimensional (2D) nanosheet with superior OER properties.[25] The desirable 2D structure is helpful to improve the percentages of exposed active metal atoms and the efficiency of charge transfer.[26] Furthermore, some drawbacks of MOFs materials, such as low yield, easy aggregation and low load, limit their practical applications.[27,28] Based on the above situation, the design of rational strategies was aimed toward obtaining the modulation of the morphology and structure for MOFs materials and achieving the water oxidation reaction.

Herein, we synthesized a series of bimetallic (Ni/Co) MOFs with 3D flower-like morphology by controlling the reaction condition and adjusting the metal ratio. In particular, the sample (F-Ni1Co4-BTC) with a Ni and Co molar ratio of 1 : 4 exhibited remarkable OER activity compared with other corresponding counterparts in alkaline solution. More noteworthy, F-Ni1Co4-BTC grown on carbon cloth as a work electrode not only improves the electrical conductivity and active sites, but also greatly guarantees the operating durability during the OER process.

Results and discussion

The formation process of F-Ni1Co4-BTC is illustrated in Fig. 1a. In the solvothermal process, the metal ions M(II) coordinated with the six O atoms of BTC to form the slightly distorted MO_6 octahedron, and the corner/edge of the MO_6 octahedron interconnected in three-dimensional space to produce the flower-like bimetallic MOF (Fig. S1†). The F-Ni*x*Co*y*-BTC crystalline structures with the different ratios of Ni/Co were studied by powder X-ray diffraction (PXRD), and are displayed in Fig. 1b. As shown in Fig. 1b, a broad diffraction signal at around 7–13° became more smooth compared to those of F-Ni-TBC (Fig. S2†) and F-Co-BTC (Fig. S3†) with the introduction of the second metal. With the reduction of the Ni/Co ratio, the main peak moved to a high diffraction angle (Fig. S4†). The amorphous structure exhibits a long-range disordered property, which was explained by the wider and lower intensity of the diffraction peak in the previous literature.[29] Therefore, the possible reason was the change of the local electron distribution and the aperiodic arrangements of the first metal atom caused by the introduction of the second metal.[30,31] The poor PXRD peaks indicated that the bimetallic MOFs had low crystallinity. Therefore, the introduction of another metal center plays an important role in reducing the crystallinity of the monometallic F-Co-BTC and F-Ni-BTC MOFs.

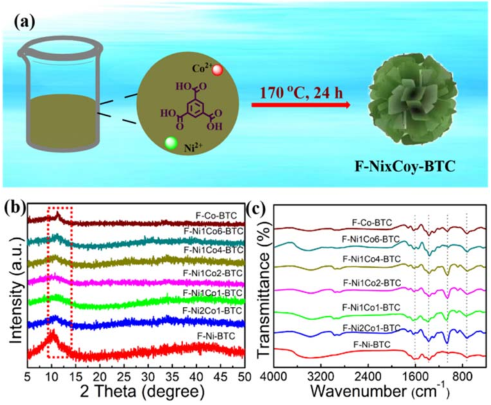

Fig. 1 (a) Schematic illustration of F-NixCo*y*-BTC, PXRD patterns (b), and FTIR spectra (c) of F-NixCo*y*-BTC.

Fourier transform infrared spectroscopy (FTIR) spectroscopy was carried out to detect the functional groups of F-Ni*x*Co*y*-BTC (Fig. 1c). The peaks at 980, 1382, and 1615 cm^{-1} were attributed to the ring-out-of-plane vibration of the 1,3,5-benzene core, the –COO– flexural vibration, and –COO– stretching vibration of the coordination bonds of organic ligand and metal centers,[32,33] respectively. The peak at 722 cm^{-1} corresponds to the vibration of the C–H bonding inside of the benzene ring.[24,34] The peak at 580 cm^{-1} was attributed to the bond between the metal atoms (Ni and Co) and the carboxylic (O–C=O) groups of BTC.[35,36] The results indicated that the coordination bond has been successfully built between the metal centre (Ni and Co) and the organic linker.

The morphology feature of F-Ni*x*Co*y*-BTC was identified by scanning electron microscope (SEM) and transmission electron microscopy (TEM). F-Ni1Co4-BTC exhibited a 3D flower-like morphology (Fig. 2a and b). The SEM images of F-Ni*x*Co*y*-BTC showed a slight change of the flower-like morphology feature with the decrease of the molar ratio of Ni/Co (Fig. S6†). Energy-dispersive X-ray spectroscopy (EDS) mapping of F-Ni1Co4-BTC displayed a uniform distribution of Ni, Co, C, and O elements (Fig. 2c). Meanwhile, the elemental composition of the F-Ni*x*-Co*y*-BTC samples was verified by EDS analytical result (Table S1†), which confirmed that the actual molar ratio of Ni and Co metals in the synthesized MOFs was close to the feeding ratios of the precursor. Furthermore, TEM images (Fig. 2d) further confirmed that F-Ni1Co4-BTC had the morphology of a 3D flower-like structure. As shown in Fig. 2e, the high-resolution transmission electron microscopy image had no obvious lattice fringes, suggesting the formation of low crystallinity.

The surface area and pore-size distribution of F-Ni1Co4-BTC was confirmed by the N_2-adsorption/desorption (Fig. 3a). The

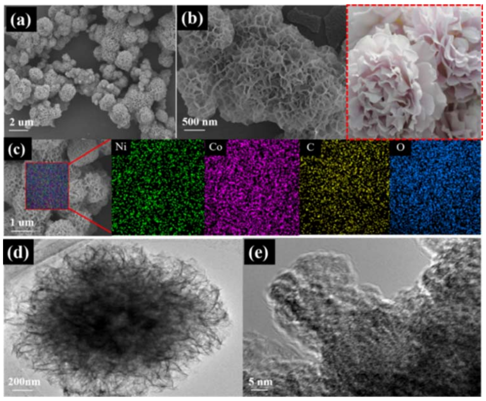

Fig. 2 (a and b) SEM images, (c) EDS element mapping images, (d) TEM image, and (e) HRTEM image of F-Ni1Co4-BTC.

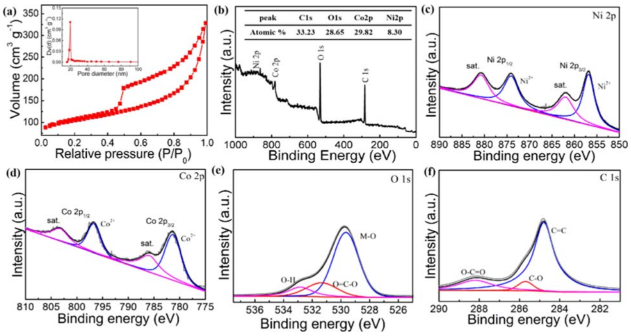

Fig. 3 N_2 adsorption–desorption isotherms and pore size distributions (a); survey XPS spectrum (b), XPS high spectra of Ni 2p (c), Co 2p (d), O 1s (e) and C 1s (f) of F-Ni1Co4-BTC.

type IV isotherms exhibited a H_3-type hysteresis ($P/P_0 > 0.4$), indicating the presence of mesopores structure. The BET surface area of F-Ni1Co4-BTC (438.9 $m^2\ g^{-1}$) obtained a remarkable promotion compared with F-Ni-BTC (181.2 $m^2\ g^{-1}$) and F-Co-BTC (226.3 $m^2\ g^{-1}$) (Fig. S7†). The pore size analysis also clearly demonstrated that the samples contained mesopores with a size distribution in the range of 15–60 nm (inset of Fig. 3a and S7†). The above structure was conducive to exposing more active sites and achieving the conversion rate of the active intermediate on the flower-like surface.

The X-ray photoelectron spectroscopy (XPS) spectra of F-Ni1Co4-BTC was carried out to further explore the electronic features of elements. The full survey spectrum confirmed the chemical composition of Ni, Co, O, and C elements (Fig. 3b), and the result was consistent with the EDS analysis. The high-resolution Ni 2p spectrum (Fig. 3c) showed the four peaks. The two main peaks of Ni $2p_{3/2}$ and Ni $2p_{1/2}$ at around 856.1 and 873.8 eV are assigned to Ni^{2+}, attributed to the formation of Ni–O bonds. The two weak peaks at around 861.5 and 879.5 eV were the satellites of Ni $2p_{3/2}$ and Ni $2p_{1/2}$, respectively.[37,38] For the Co 2p XPS spectrum (Fig. 3d), the presence of Co^{2+} was determined by Co $2p_{3/2}$ (781.3 eV) and Co $2p_{1/2}$ (796.5 eV), and the peaks at 786.1 (Co $2p_{3/2}$) and 803.3 eV (Co $2p_{1/2}$) are satellite features.[39,40] The O1s spectrum (Fig. 3e) exhibited three energy peaks at 529.8, 531.8 and 532.9 eV, which were ascribed to the Ni(Co)–O bands, the oxygen components (O=C–C) of the BTC liners, and the absorbed water molecules, respectively.[21,24,41,42] The higher C 1s spectrum (Fig. 3f) showed the coexistence of three surface components, which were the benzoic ring (284.8 eV), C–O (285.7 eV), and carboxylate (O–C=O) group of BTC (288.3 eV),[43,44] respectively. All of these analysis results further confirmed that the incorporation of metal ions (Ni^{2+} and Co^{2+}) and BTC ligands resulted in the formation of bimetallic F-Ni1Co4-BTC.

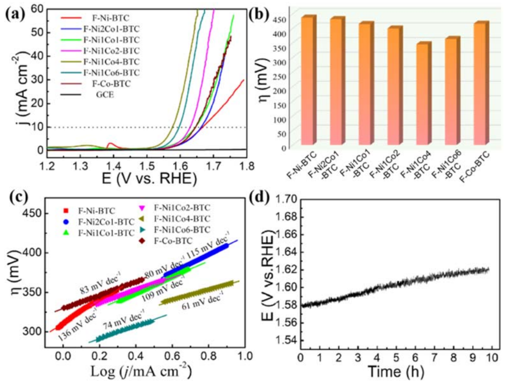

Fig. 4 LSV polarization curves (a) and (b) the contrast of the overpotential (*vs.* materials of different Ni/Co ratios) at a current density of 10 mA cm^{-2}, (c) corresponding Tafel plots of F-NiCo-BTC. (d) Chronoamperometry responses of F-Ni1Co4-BTC under a current density of 10 mA cm^{-2} over 10 h.

To investigate the electrochemical performance of catalysts for OER, as-obtained samples were drop-casted on the surface of the glassy carbon electrode (GCE) as the working electrode in a three-electrode system at pH ~14 (1.0 M KOH solution). All of the linear sweep voltammetry (LSV) curves were *iR*-corrected, ascribed to the ohmic potential drop losses from the solution resistance (Fig. S8†). As shown in Fig. 4a, the GCE displayed a negligible OER activity,[45,46] and a coating of catalyst obviously enhanced the catalytic activity. The LSV curves showed that F-Ni1Co4-BTC possessed the highest current density. The overpotential (η_{10}) of F-Ni1Co4-BTC was only 343 mV at a current density of 10 mA cm^{-2}, which was smaller than other bimetallic samples in the same current density (Fig. 4b), indicating the superior OER activity of F-Ni1Co4-BTC. The Tafel slopes come from the corresponding linear fitting of polarization curves by the Tafel equation: $\eta = \log j + a$ (where η is the overpotential, j is the current density, and b is the Tafel slope).[35] F-Ni1Co4-BTC displayed the lowest Tafel slope (61 mV dec^{-1}), corresponding to the fastest OER kinetics among all of the F-Ni*x*Co*y*-BTC MOFs (Fig. 4c), which indicated the outstanding reaction kinetics. The disordered coordination of the Ni and Co ions with BTC resulted in the reduced crystallinity and the improved surface area, which were beneficial to expose richer metal active sites. The excellent OER activity of F-Ni1Co4-BTC may have benefited from the synergistic action of Ni^{2+} and Co^{2+} and the exposed richer metal active sites. To confirm the practicability of the catalyst, the long-term stability of F-Ni1Co4-BTC on GCE was examined under a constant current density of 10 mA cm^{-2} in 1.0 M KOH solution for at least 10 h. As shown in Fig. 4d, the chronopotentiometry value clearly increased from the initial required potential of 1.573 to 1.618 V *versus* RHE over 10 h. The reason for the slight decay was a weak mechanical binding between the F-Ni1Co4-BTC powder and GCE. Even if Nafion served as a binder, some catalyst would be shed from the surface of the working electrode over time.

After confirming F-Ni1Co4-BTC as the most active sample, we tried to optimize the catalytic activity and mechanical stability of the electrode. F-Ni1Co4-BTC was directly grown on the high surface area of a carbon cloth substrate (denoted as F-Ni1Co4-BTC/CC). The structure, morphology and element composition of F-Ni1Co4-BTC/CC were confirmed by means of PXRD pattern, SEM images, elemental maps, and EDS spectrum (Fig. S9†). Furthermore, the OER performance and stability of the F-Ni1Co4-BTC/CC electrode were assessed by employing the above-mentioned methods. The assembled electrode achieved an η_{10} of 292 mV and a low Tafel slope of only 48 mV dec^{-1}, which was comparable to the commercial RuO_2 catalyst (Fig. 5a and b). Electrochemical impedance spectra (EIS) were obtained from 1 mHz to 100 kHz under a potential of 1.54 V *versus* RHE. The Nyquist plots are depicted in Fig. 5c. The R_s and R_{ct} mainly result from the electrolyte resistance and interfacial charge transfer resistance, respectively. F-Ni1Co4-BTC/CC exhibited a much lower R_{ct} of 9.1 Ω cm^2 compared with F-Ni1Co4-BTC (23.1 Ω cm^2) and CC (10.6 Ω cm^2). The high-efficiency charge transport performance of the integrated electrode came from the introduction of high conductive substrates (CC), which was beneficial to achieve the higher faradaic process and OER kinetics. Moreover, the double-layer capacitance (C_{dl}) was applied to obtain the electrochemically active surface area (ECSA) by the cyclic voltammogram (CV) curves with various scan rates in a potential range of 1.0–1.1 V (Fig. S10†). The C_{dl} value of the F-Ni1Co4-BTC/CC electrode was 23.4 mF cm^{-2}, which was 2.2 times that of F-Ni1Co4-BTC (10.4 mF cm^{-2}), and 5.2 times that of CC (4.5 mF cm^{-2}). The high C_{dl} value indicated that the effective active sites were significantly increased due to the incorporation of F-Ni1Co4-BTC with CC (Fig. 5d). In addition, the mass activity and values of the turnover frequency (TOF) were calculated using the following equation to evaluate the intrinsic electrochemical activity:[45,47]

$$\text{Mass activity} = j/m \tag{1}$$

$$\text{TOF} = (jA)/(4Fn) \tag{2}$$

where j (A cm^{-2}), m (g cm^{-2}), and A (cm^{-2}) denote the current density at a given overpotential (200 mV *vs.* RHE), the mass of the loading catalyst, and the surface area of the electrode, respectively. The number 4 represents that the transfer of 4 electrons is needed for generating one O_2 molecule. F (96 485.3 C mol^{-1}) is the Faraday constant, and n denotes the number of moles of metal atoms. The mass activity and TOF values of F-Ni1Co4-BTC at η of 200 mV *vs.* RHE were checked (Table 1). The calculated mass activity (15.63 A g^{-1}) and TOF (0.0117 s^{-1}) values of F-Ni1Co4-BTC/CC outperformed that of F-Ni1Co4-BTC and RuO_2 modified with GCE, which indicated that F-Ni1Co4-BTC/CC possessed an optimal intrinsic catalytic activity for the OER. The above results indicated that F-Ni1Co4-BTC grown on CC achieved an effective optimization of OER catalyst activity. The performance of the as-prepared 3D assembled electrode was superior to that of the other recently reported MOF-based electrodes (Table S2†). Lastly, the F-Ni1Co4-BTC/CC electrode exhibited effective durability compared with the F-Ni1Co4-BTC powder embellished on GCE for OER electrocatalytic property. The chronoamperometry curve (red, left) kept a steady current density, which presented a slight potential drop from 30.1 to 29.4 mA cm^{-2} at the constant overpotential of 1.566 V *vs.* RHE over 10 h in 1.0 M KOH electrolyte. Meanwhile, the chronopotentiometry curve (blue, right) exhibited a slight increase of 1.8% (the change of potential value from 1.527 to 1.553 V *vs.* RHE) under a current density of 10 mA cm^{-2} with 10 h (Fig. 5e). In addition, the polarization curves after 1000 cycles showed an almost similarity with the initial polarization curve (Fig. 5f), and SEM images of the F-Ni1Co4-BTC/CC composite before and after 1000 cycles displayed a negligible change (inset of Fig. 5f).

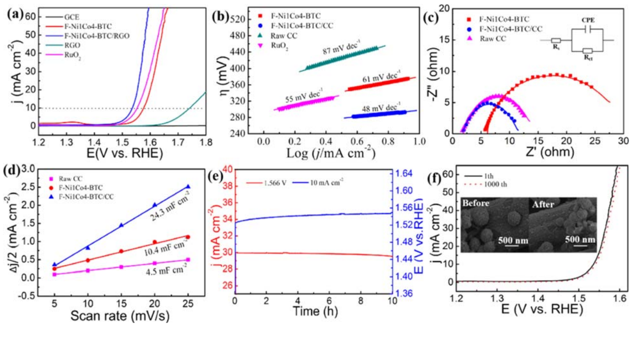

Fig. 5 OER performance of F-Ni1Co4-BTC decorated on different electrodes in 1.0 M KOH solution. (a) LSV polarization curves, (b) corresponding Tafel plot coming from (a) curves, and (c) electrochemical impedance at 1.54 V *vs.* RHE under similar conditions. (d) Plots used to extract double-layer capacitances (C_{dl}) based to CV curves at different scan rates. Stability evolution of the F-Ni1Co4-BTC/CC electrode: (e) I–t curve (red) at a constant voltage of 1.566 V (*vs.* RHE) and E–t curve (blue) at a current density of 10 mA cm^{-2}, and (f) comparison of the LSV curves and SEM images for 1000 cycles.

To investigate the electrocatalytic mechanisms of the MOF for the OER, XPS was carried out to reveal the phase transformation of the F-Ni1Co4-BTC/CC composite before and after the OER cycling. The Ni 2p spectrum (Fig. 6a) clearly displays a negative shift of the peak location (0.8 eV) for Ni $2p_{3/2}$ and $2p_{1/2}$, ascribed to the change of the local electronic structure of Ni after the destruction of organic ligands in the OER process, among the peaks at 850.1 and 872.5 eV belonging to the presence of NiO for the Ni^{2+} species.[41] Moreover, the weak peaks at around 856.4 and 874.1 eV indicated the existence of Ni^{3+}, due to the formation of NiOOH during the water oxidation process. Similarly, compared to the results from before OER cycling, a negative shift of the peaks for the Co^{2+} species (Co $2p_{3/2}$: 795.8 eV; Co $2p_{3/2}$: 780.6 eV) occurred (Fig. 6b). Furthermore, there is the generation of new peaks (897.2 and 786.3 eV) belonging to the Co^{3+} species. These changes are ascribed to the formation of CoO and CoOOH during the OER process.[49] In addition, the distinct shift of the dominant peak for O 1s is attributed to the formation of the oxygen species (M–O–M) and hydroxyl groups (M–OOH).[50] The above results suggested the formation of Ni–O–Ni (Co–O–Co) and NiOOH (CoOOH) on the surface of the catalyst after OER process.[51,52] The above analysis results verified the structural shrinkage of the MOFs, accompanied with the destruction of the organic ligand BTC during water oxidation. This resulted in the presence of the interconnected NiO/CoO and NiOOH/CoOOH acting as the more active phase.[37,53]

The excellent OER activity of the F-Ni1Co4-BTC/CC electrode can be derived from the following aspects: (I) the formation of the flower-like morphology ensures the high specific surface area and ample pores of the integrated electrode (Fig. 6d), which could provide the desirable mass transport for the abundant active species. (II) The existence of the CC promotes

Table 1 Summary of the electrochemical properties for the F-Ni1Co4-BTC sample

Catalyst	η @ $J = 10$ mA cm^{-2} (mV)	Tafel slope (mV dec^{-1})	R_{ct} (Ω cm^2)	C_{dl} (mF cm^{-2})	Mass activity (A g^{-1})	TOF (s^{-1})
F-Ni1Co-BTC	343	87	23.1	10.4	6.25	0.0054
F-Ni1Co4-BTC/CC	292	48	9.1	23.4	15.63	0.0117
RuO_2	319	55	—	11.7 (ref. 48)	9.68	0.0073

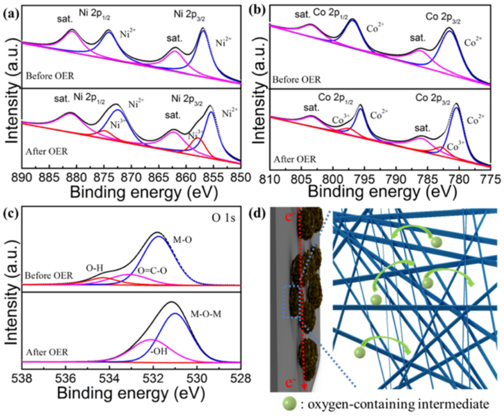

Fig. 6 High-resolution XPS spectra of (a) Ni 2p, (b) Co 2p and (c) O 1s for the F-Ni1Co4-BTC material before and after OER testing. (d) Illustration of the OER catalytic process for the Ni1Co4-BTC@CC electrode.

electronic conductivity and accelerates the reaction kinetics (Fig. 5b and 6d). (III) The formation of the M–O–M and MOOH multiple active species provides more active sites during the OER process. According to the above discussion, this controllable and feasible design is an effective strategy to perfect the activity and durability of the bimetallic MOFs material.

Conclusions

In summary, 3D flower-like bimetallic (Ni/Co) MOFs were successfully designed and prepared *via* introducing the second metal element into Ni-BTC and Co-BTC. The optimized bimetallic F-Ni1Co4-BTC is more active than monometallic F-Ni-BTC and F-Co-BTC for the OER process. The outstanding catalytic activity of F-Ni1Co4-BTC was attributed to the synergistic effect of the Ni^{2+} and Co^{2+} with an optimal ratio and the low crystallinity in the bimetallic F-Ni*x*Co*y*-BTC system, which were beneficial in exposing richer active sites. Moreover, F-Ni1Co4-BTC fixed on the surface of carbon cloth realized high OER activity and long-time durability. Specifically, the integrated electrode provided rich active sites, convenient transfer channels, and fast electronic conductivity during the OER process. The promising results will promote the development of bimetallic MOFs as efficient catalysts for the energy conversion process.

Conflicts of interest

The authors declare that they have no known competing financial interests or personal relationships that could have appeared to influence the work reported in this paper.

Acknowledgements

This work was supported by the Natural Science Foundation of China (22365027); the College Industry Support Plan Project of Gansu Province (No. 2023CYZC-12); Higher Education Technology Innovation Project of Gansu Province (No. 2023B-203, 2024A-164); Doctoral Start-up Founds from Gansu Provincial Department of Education (2023QB-016); Doctoral Start-up Founds from Longdong University (No. XYBYZK2101); and the Youth Science and Technology Foundation of Qingyang City (No. QY-STK-2022A-013).

Notes and references

1 N. T. Suen, S. F. Hung, Q. Quan, N. Zhang, Y. Xu and H. M. Chen, *Chem. Soc. Rev.*, 2017, **46**, 337–365.
2 A. Munir, K. S. Joya and I. Hussain, *ChemSusChem*, 2019, **12**, 1517–1548.
3 M. A. Green and S. P. Bremner, *Nat. Mater.*, 2017, **16**, 23–34.
4 S. Fu, J. S, C. Zhu, G. Xu, K. Amine, C. Sun and Y. Lin, *Nano Energy*, 2018, **44**, 319–326.
5 T. T. H. Hoang and A. A. Gewirth, *ACS Catal.*, 2016, **6**, 1159–1164.
6 U. Khan, A. Nairan, J. Gao and Q. Zhang, *Small Struct.*, 2023, **6**, 2200109.
7 P. Chen, K. Xu, T. Zhou, Y. Tong, J. Wu, H. Ding and Y. Xie, *Angew. Chem., Int. Ed.*, 2016, **128**, 2534–2538.
8 Z. Li, H. He, H. Cao, S. Sun, W. Diao, D. Gao, P. Lu, S. Zhang, Z. Guo, J. Jiang and G. Zhang, *Appl. Catal., B*, 2019, **240**, 112–121.
9 C. McCrory, S. Jung, J. Peters and T. Jaramillo, *J. Am. Chem. Soc.*, 2013, **135**, 16977–16987.
10 J. Ding, X. Zhu, H. Pei, S. He, R. Yang, N. Liu, R. Guo and Z. Mo, *Int. J. Hydrogen Energy*, 2023, **48**, 17468–17747.
11 Y. Pi, N. Zhang, S. Guo, J. Guo and X. Huang, *Nano Lett.*, 2016, **16**, 4424–4430.
12 Z. Li, X. Dou, Y. Zhao and C. Wu, *Inorg. Chem. Front.*, 2016, **3**, 1021–1027.
13 W. Liu, Y. Hou, Z. Lin, S. Yang, C. Yu, C. Lei, X. Wu, D. He, Q. Jia, G. Zheng, X. Zhang and L. Lei, *ChemSusChem*, 2018, 1479–1485.

14 K. Zhu, H. Liu, M. Li, X. Li, J. Wang, X. Zhu and W. Yang, *J. Mater. Chem. A*, 2017, **5**, 7753–7758.

15 Y. Yang, L. Dang and M. J. Shearer, *Adv. Energy Mater.*, 2018, **8**, 1703189.

16 X. Zhang, J. Luo, P. Tang, X. Ye, X. Peng, H. Tang, S. G. Sun and J. Fransaer, *Nano Energy*, 2017, **31**, 311–321.

17 T. D. Bennett and A. K. Cheetham, *Acc. Chem. Res.*, 2014, **47**, 1555–1562.

18 F. Y. Yi, R. Zhang, H. Wang, L. F. Chen, L. Han, H. L. Jiang and Q. Xu, *Small Methods*, 2017, **1**, 1700187.

19 M. Zhang, Q. Dai, H. Zheng, M. Chen and L. Dai, *Adv. Mater.*, 2018, **30**, 1705431.

20 X. Xiao, C. T. He, S. Zhao, J. Li, W. Lin, Z. Yuan, Q. Zhang, S. Wang, L. Dai and D. Yu, *Energy Environ. Sci.*, 2017, **10**, 893.

21 K. Rui, G. Zhao, Y. Chen, Y. Lin, Q. Zhou, J. Chen, J. Zhu, W. Sun, W. Huang and S. Dou, *Adv. Funct. Mater.*, 2018, **28**, 1801554.

22 F. L. Li, Q. Shao, X. Huang and J. P. Lang, *Angew. Chem., Int. Ed.*, 2018, **57**, 1888.

23 J. Shen, P. Liao, D. Zhou, C. He, J. Wu, W. Zhang, J. Zhang and X. Chen, *J. Am. Chem. Soc.*, 2017, **139**, 1778–1781.

24 J. Li, W. Huang, M. Wang, S. Xi, J. Meng, K. Zhao, J. Jin, W. Xu, Z. Wang, X. Liu, Q. Chen, L. Xu and L. Mai, *ACS Energy Lett.*, 2018, **4**, 285–292.

25 S. Zhao, Y. Wang, J. Dong, C.-T. He, H. Yin, P. An, K. Zhao, X. Zhang, C. Gao, L. Zhang, J. Lv, J. Wang, J. Zhang, A. M. Khattak, N. A. Khan, Z. Wei, J. Zhang, S. Liu, H. Zhao and Z. Tang, *Nat. Energy*, 2016, **1**, 16184.

26 L. Zhuang, L. Ge, H. Liu, Z. Jiang, Y. Jia, Z. Li, D. Yang, R. K. Hocking, M. Li, L. Zhang, X. Wang, X. Yao and Z. Zhu, *Angew. Chem., Int. Ed.*, 2019, **58**, 287.

27 M. Jahan, Z. Liu and K. P. Loh, *Adv. Funct. Mater.*, 2013, **23**, 5363.

28 D. Kim and A. Coskun, *Angew. Chem., Int. Ed.*, 2017, **56**, 5071–5076.

29 H. Wu, S. Huang, F. Ding, Y. Ma, Q. Zhai, Y. Ren, Y. Yang, L. Chen, S. Tang and X. Meng, *J. Phys. Chem. C*, 2022, **126**, 19715–19725.

30 T. D. Bennett and A. K. Cheetham, *Acc. Chem. Res.*, 2014, **47**, 1555–1562.

31 J. L. Mancuso, A. M. Mroz, K. N. Le and C. H. Hendon, *Chem. Rev.*, 2020, **120**, 8641–8715.

32 A. Rajan, M. D. Dhileepan, S. Kamalakannan, M. Prakash, S. Krishnamurthy and B. Neppolian, *ACS Appl. Energy Mater.*, 2023, **6**, 9207–9217.

33 L. Gou, L. Hao, Y. Shi, S. Ma, X. Fan, L. Xu, D. Li and K. Wang, *J. Solid State Chem.*, 2014, **210**, 121–124.

34 Y. Wang, Q. Qu, G. Liu, V. S. Battaglia and H. Zheng, *Nano Energy*, 2017, **39**, 200–210.

35 F. Sun, G. Wang, Y. Ding, C. Wang, B. Yuan and Y. Lin, *Adv. Energy Mater.*, 2018, **8**, 1800584.

36 G. Zou, X. Jia, Z. Huang, S. Li, H. Liao, H. Hou, L. Huang and X. Ji, *Electrochim. Acta*, 2016, **196**, 413–421.

37 K. Rui, G. Zhao, Y. Chen, Y. Lin, Q. Zhou, J. Chen, J. Zhu, W. Sun, W. Huang and S. X. Dou, *Adv. Funct. Mater.*, 2018, **28**, 1801554.

38 S. Zhao, C. Gao, L. Zhang, J. Lv, J. Wang, J. Zhang, A. M. Khattak, N. A. Khan, Z. Wei, J. Zhang, S. Liu, H. Zhao and Z. Tang, *Nat. Energy*, 2016, **1**, 1–12.

39 H. Yu, L. Wang, H. Li, Z. Luo, T. T. Isimjian and X. Yang, *Chem. - Eur. J.*, 2022, **28**, e202201784.

40 C. Li, X. Lou, M. Shen, X. Hu, Z. Guo, Y. Wang, B. Hu and Q. Chen, *ACS Appl. Mater. Interfaces*, 2016, **8**, 15352–15360.

41 T. Tian, L. Huang, L. Ai and J. Jiang, *J. Mater. Chem. A*, 2017, **5**, 20985–20992.

42 C. Li, X. Hu, W. Tong, X. Lou, M. Shen and B. Hu, *ACS Appl. Mater. Interfaces*, 2017, **9**, 29829–29838.

43 M. A. Peck and M. A. Langell, *Chem. Mater.*, 2012, **24**, 4483–4490.

44 R. Wang, C. Xu and J. M. Lee, *Nano Energy*, 2016, **19**, 210–221.

45 Q. Dong, C. Shuai, Z. Mo, Z. Liu, G. Liu, J. Wang, Y. Chen, W. Liu, N. Liu and R. Guo, *New J. Chem.*, 2020, **44**, 17744.

46 L. Ai, T. Tian and J. Jiang, *ACS Sustainable Chem. Eng.*, 2017, **5**, 4771–4777.

47 N. Srinivasa, J. P. Hughes, P. S. Adarakatti, C. Manjunatha, S. J. Rowley-Neale, S. Ashoka and C. E. Banks, *RSC Adv.*, 2021, **11**, 14654.

48 L. Zhang, H. Jang, H. Liu, M. G. Kim, D. Yang, S. Liu, X. Liu and J. Cho, *Angew. Chem., Int. Ed.*, 2021, **16**, 18969–18977.

49 X. Zhao, B. Pattengale, D. Fan, Z. Zou, Y. Zhao, J. Du, J. Huang and C. Xu, *ACS Energy Lett.*, 2018, **3**, 2520–2536.

50 Y. Dang, P. Han, Y. Li, Y. Zhang and Y. Zhou, *J. Mater. Sci.*, 2022, **55**, 13951–13963.

51 H. Y. Wang, Y. Y. Hsu, R. Chen, T. S. Chan, H. M. Chen and B. Liu, *Adv. Energy Mater.*, 2015, **5**, 1500091.

52 Y. Fan, J. Zhang, K. Luo, X. Zhou, W. Bao, H. Su, N. Wang, P. Zhang and Z. Luo, *Inorg. Chem. Front.*, 2024, **11**, 114–122.

53 Q. Gan, B. Liu, K. Zhao, Z. He and S. Liu, *Electrochim. Acta*, 2018, **279**, 152–160.